Geometry and Local Environment of Surface Sites in Vanadium-based Ziegler-Natta Catalysts from ^{51}V solid-state NMR Spectroscopy

Sebastian Sabisch‡, Yuya Kakiuchi‡, Scott R. Docherty, Alexander V. Yakimov, Christophe Copéret*

ETH Zürich, Department of Chemistry and Applied Biosciences, Vladimir Prelog Weg 1-5, 8093 Zurich, Switzerland

$MgCl_2$, Ziegler-Natta Catalysts, ^{51}V NMR, Vanadium, surface sites, Activated $MgCl_2$, solid-state NMR, polymerization catalyst

ABSTRACT: Since its emergence over 50 years ago, the structure of surface sites in Ziegler-Natta catalysts, which are responsible for a major fraction of the world's supply of polyethylene (PE) and polypropylene (PP), has remained elusive. This is in part due to the complexity of the systems that involve multiple synthetic steps and components, namely the $MgCl_2$ support, a transition-metal chloride, and several organic modifiers, known as donors, that are used prior and in some instances during the activation step with alkyl aluminum. Due to the favorable NMR properties of V and its use in Ziegler-Natta catalysts, we utilize ^{51}V solid-state NMR spectroscopy to investigate the structure of $VOCl_3$ on $MgCl_2(thf)_{1.5}$. The resulting catalyst shows similar ethylene polymerization activity as its Ti analogues. Using carefully benchmarked DFT calculations, the experimental ^{51}V NMR signature was analyzed to elucidate the structure of the surface sites. Using this approach, we demonstrate that the ^{51}V NMR signature contains information about the coordination environment, i.e. the type of ancillary, ligands and the morphology of the $MgCl_2$ support. Analysis of the NMR signatures shows that the adsorption of $VOCl_3$ on $MgCl_2(thf)_{1.5}$ generates a well-defined hexacoordinated V-oxo species containing one alkoxy and four chloride ligands, whose local geometry results from the interaction with an amorphous $MgCl_2$ surface. This study illustrates how NMR spectroscopy, which is highly sensitive to the local environment of the investigated nuclei, here V, enables us to identify the exact coordination sphere and to address the effect of support morphology on surface site structures.

INTRODUCTION

Heterogeneous Ziegler-Natta catalysts (ZNC) are textbook industrial catalysts that have changed polyolefin synthesis and enabled to obtain of a broad range of polymer properties upon small changes of the catalyst composition. They have nowadays reached multi-million ton-a-year processes[1] for the production of ranges of polyethylene and polypropylene. The development of ZNCs has been empirically driven since their emergence in the 1960s, with the use of various organic additives at the different stages of the synthesis of the catalysts (e.g. internal or external donors, e.g. THF, ethanol, esters, ethers…) and alternative metals (V ,[2] Fe,[3-4] Cr,[3] Zr,[5] …). A key component, that is found in all industrial ZNCs, is "activated" $MgCl_2$, a support that proves crucial for polymerization performances and the final polymer properties. Multiple parameters greatly influence the activity of such multicomponent catalysts and the final property of the polymer, hence the popularity of these catalysts in industry.[6-8] After years of research, focusing mostly on Ti-based ZNCs, the role of the $MgCl_2$ support and various additives on the structure of the active sites remains mostly unclear. The lack of sensitive and accessible characterization methods has slowed down the elucidation of these pre-catalysts, preventing detailed and meaningful structure-activity relationships in ZNCs to be established.[9] In fact, the very nature of the interactions between the metal sites and $MgCl_2$ remains unknown.

The preparation of ZNCs typically involves three key steps: i) the activation of $MgCl_2$ either chemically (e.g. by addition of THF, ethanol, or other internal donors) or physically (e.g. ball-milling), ii) the dispersion of the transition-metal halide (e.g. $TiCl_4$) on the activated $MgCl_2$ support yielding a pre-catalyst, and finally, iii) the activation of the pre-catalysts with alkyl Al compounds, like $AlEt_3$;[8] this last step can be carried out with or without additional additives. Titanium is the most abundantly used transition metal element for ZNC, which contrasts the wider variety of transition metals used for the corresponding homogeneous polymerization catalysts.[10] The corresponding V-based ZNCs have also been developed and are used in the polymerization of ethylene and propylene as well as in the copolymerization of ethylene with larger terminal olefins such as 1-hexene.[11-12]

While the active species only form upon reaction with $AlEt_3$, the initial state of the supported metal species (pre-catalyst) is extremely important in determining the activity and selectivity of these catalysts. Yet, even at this stage of the catalyst preparation, the nature of the surface species remains unknown. Therefore, understanding the surface adsorption sites of the support, namely the coordination environment of the transition metal (geometry, type of ligand, adsorption sites) is crucial. Towards this goal, a wide range of spectroscopic and computational methods have been employed, with studies focusing mostly on Ti-based systems.[9, 13-19] Most of them point to the interaction of Ti with undercoordinated Mg surface species. The Ti-sites are typically described as adopting a near octahedral geometry and containing mostly Cl ligands. One of the key challenges in assessing these structures is the diffraction amorphous structure of the activated $MgCl_2$ support itself.[20-21]

The chemical activation and dispersion of the metal complex (e.g. $TiCl_4$) on $MgCl_2$ leads to a loss of the long-range order of the support, making characterization methods such as powder X-ray diffraction challenging.[19-23] Detailed investigations of pre-catalysts by ^{13}C NMR spectroscopy have shown that upon adsorption some of the Cl ligands bound to Ti can be partially substituted by alkoxides coming from the internal donor, illustrating that the support is not innocent.[14] Recent studies have shown that a pre-treatment with BCl_3 can remove these alkoxide ligands and increase the catalysts activity after activation with $AlEt_3$ due to an increased number of active sites.[16] Detailed study of this system using a combination of EPR and DFT calculations has demonstrated that the active species correspond to bi-metallic Ti-Al alkyl species,[14, 16] confirming earlier mechanistic proposals (Rodriguez–Van Looy mechanism).[24] Despite these advances, the role of the support and the nature of the Ti-species in the pre-catalyst remains unknown and is particularly challenging for spectroscopic methods such as X-Ray absorption or Ti-NMR spectroscopies.[17-18, 25]

Given the related reactivity of V-based ZNC and the highly favorable NMR properties of ^{51}V (> 99% natural abundance and high gyromagnetic ratio resulting in a receptivity compared to ^{13}C of > 10^3), we hypothesized that understanding the nature of the V sites by ^{51}V NMR could be an ideal method to probe the structure of the metal sites on $MgCl_2$.[26] Indeed, the transition-metal chloride precursors, $TiCl_4$ and $VOCl_3$, are formally isoelectronic and can in principle adsorb on similar sites, hence information about the metal-support interaction obtained with V can be useful for Ti-based catalysts. Moreover, ^{51}V benefits from being a quadrupolar nucleus (I = 7/2) with a relatively small quadrupole moment compared to Ti (^{51}V = -0.043 b vs. ^{47}Ti = 0.30 b and ^{49}Ti = 0.24 b)[27] and having a large chemical shift range (~2000 ppm), thus ennobling excellent sensitivity towards small changes in the environment of the nucleus without the need for complex excitation schemes. Such an approach is currently very challenging for $^{47/49}Ti$ [28], especially at low metal content.[29-31] In this work, we decided to focus on $VOCl_3$@$MgCl_2(thf)_{1.5}$ because of the large set of experimental data for the corresponding Ti systems, $TiCl_4$@$MgCl_2(thf)_{1.5}$.[2, 14, 32] By confronting experimental ^{51}V NMR spectra with calculated NMR data obtained from computational models, we elucidate the coordination environment, local geometry and the interacting surface sites of $MgCl_2$.

RESULTS

The V-based Ziegler-Natta catalyst (V-ZNC) is prepared via interaction of $VOCl_3$ with $MgCl_2(thf)_{1.5}$ support in toluene at elevated temperatures (90 °C), similarly to the corresponding Ti-systems,[14] yielding a catalyst $VOCl_3$@$MgCl_2(thf)_{1.5}$ which contains both unreacted and ring opened THF (For preparation detail, see ESI). The V-loading is between 2.96 and 4.64 $\%_{wt}$, which is similar to the corresponding Ti-ZNC prepared via the same approach.[18] The composition of the catalyst is determined by elemental analysis of Mg, Cl and C, as $(VOCl_3)_{0.14}MgCl_2(thf)_{0.71}$, showing that a significant amount of THF has been displaced. X-ray powder diffraction analysis exhibited a significant broadening of the features upon treatment of $MgCl_2(thf)_{1.5}$ with $VOCl_3$, which is consistent with the observed increase of the surface area from 5.2 m^2/g to 50 m^2/g, both indicating a loss of long range order (> 2 nm) compared to its pristine state, also paralleling what is observed for the corresponding Ti-based systems (ESI).[33] The solid displays a catalytic activity of 4.7 $kg_{PE}\cdot g_V^{-1}\cdot h^{-1}$ in ethylene polymerization reaction under standard conditions (20 bar of ethylene, 30 °C, *n*-heptane as solvent) upon activation with $AlEt_3$,paralleling the reactivity of the Ti-based systems. Coming back to characterization, the solid-state ^{13}C NMR spectrum is dominated by two features at 70 and 28 ppm corresponding to residual THF coordinated to the surface of $MgCl_2$, while the IR spectrum shows the emergence of peak at ca. 750 cm^{-1} reminiscent of a C-Cl bond resulting from the ring opening of THF (ESI).

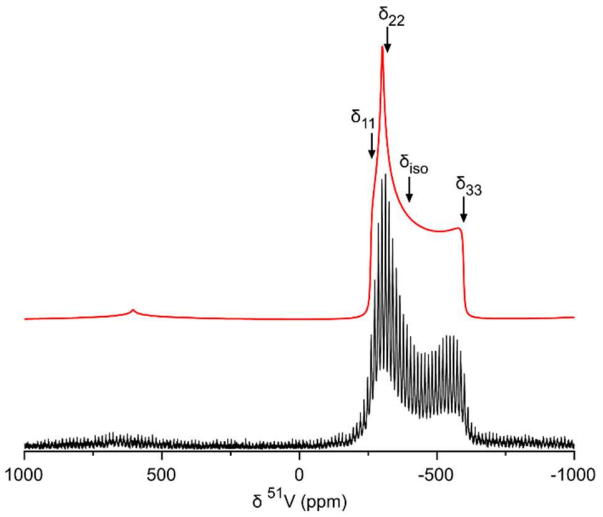

Figure 1. Static ^{51}V NMR spectrum of $VOCl_3$@$MgCl_2(thf)_{1.5}$ acquired at 103 K at 14.1 T using WURST-QCPMG pulse sequence with the corresponding simulated line shape depicted red. Fitting of the single NMR line yielded δ_{11} = -268, δ_{22} = -319, and δ_{33} = -598 ppm, while the C_Q (5-10 MHz) and η (~0.5) could only be estimated.

We next analyzed this pre-catalyst using static ^{51}V solid-state NMR (ssNMR) spectroscopy. Using the WURST-QCPMG pulse sequence,[34-36] we obtained a high-quality spectrum with a good signal-to-noise ratio of 150 within 12 hours at 103 K (reasonable S/N ratios can be obtained within minutes). The ^{51}V ssNMR of the pre-catalyst shows a well-defined NMR line shape with an isotropic chemical shift ($\delta_{iso} = (\delta_{11} + \delta_{22} + \delta_{33})/3$) of -395 ppm (Figure 1). Variation of the magic angle spinning rates was used to identify spinning sidebands and determine the isotropic chemical shift and reveals that the spectrum is consistent with a single spectral signature. The quadrupolar nature of ^{51}V can be observed as evidenced by minor second-order broadening and a satellite transition at 600 ppm. This distortion is sufficient to evaluate the parameters associated with the electric field gradient, namely the quadrupolar coupling constant C_Q ($C_Q = eQV_{zz}/h$) of ~8 MHz, and asymmetry parameter η ($\eta = (V_{xx}-V_{yy})/V_{zz}$, $|V_{zz}| \geq |V_{xx}| \geq |V_{yy}|$) of ~0.5.

Notably, the overall linewidth is dominated by the span of the chemical shift tensor ($\Omega = \delta_{11} - \delta_{33}$ = 330 ppm), thus allowing us to only consider chemical shift anisotropy to further analyze the spectrum. Fitting of NMR spectra obtained at various conditions (ESI) grants access to the complete chemical shift tensor and its components (δ_{11} = –268, δ_{22} = –319, and δ_{33} = –598 ppm). The similarity between δ_{11} and δ_{22} indicates a near-axial symmetry of the surface site(s) as revealed by the skew κ ($\kappa = 3(\delta_{22}-\delta_{iso})/\Omega$) of 0.7.

To allow for a more detailed interpretation of the experimental NMR data, we investigated a series of DFT models of potential surface sites of $VOCl_3$@$MgCl_2(thf)_{1.5}$ to confront experimental

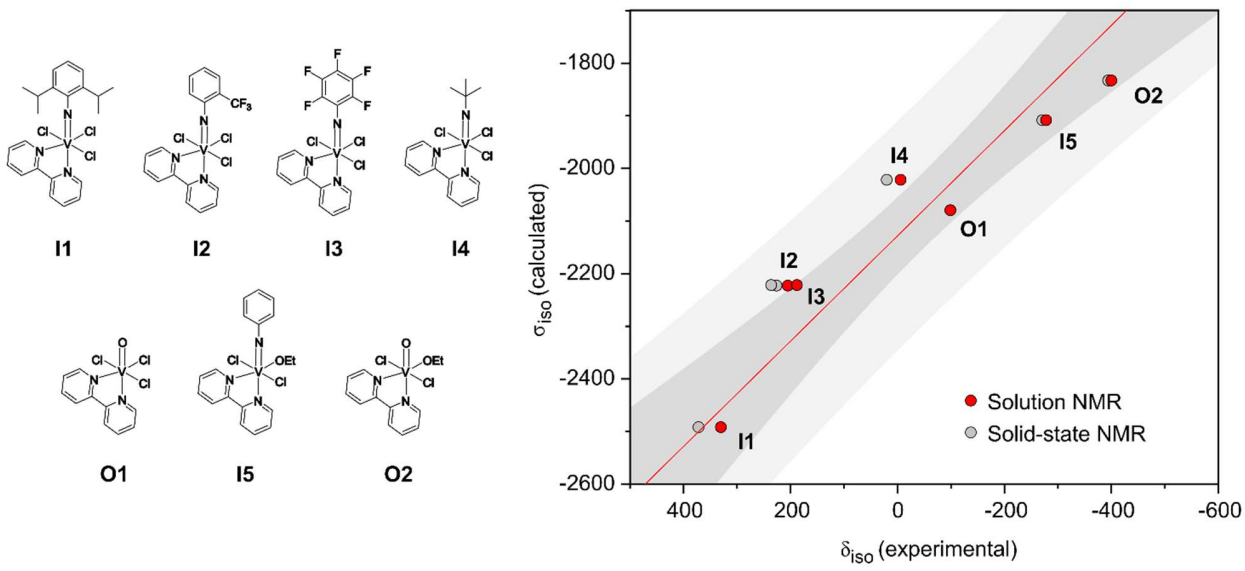

Figure 2. Calculated δ_{iso} of a series of imido and oxo vanadium complexes compared to the experimentally determined ^{51}V chemical shift collected in C_6D_6 shown in red and from solid-state NMR shown in grey. The experimental and calculated data show a linear correlation. The respective linear fit to the solution NMR data is shown in red, with the 95% confidence and 95% prediction intervals shown in light and dark grey respectively. The solid-state NMR data shows a systematic offset to the solution NMR data accounted to the concentration dependence of the reference.

with calculated NMR spectra. To benchmark our NMR calculations, we used a library of molecular compounds.

Regarding the models of surface sites, we consider three main parameters with increasing complexity: i) the adsorption of $VOCl_3$ on various well-defined surface sites, expected from specific facets of crystalline $MgCl_2$ (as typically investigated) [13, 37] ii) the introduction of alkoxide ligands bound to V as previously discussed for the corresponding Ti-ZNC[14] due to the possible reaction of the vanadium precursor ($VOCl_3$) with the adsorbed THF found in $MgCl_2(thf)_{1.5}$ iii) the evaluation of distortion at the $MgCl_2$ surface sites due to amorphization.

Prior to surface-site evaluation, we first benchmark the ^{51}V NMR calculations by comparing experimental and calculated NMR parameters for a series of tailored monomeric, octahedral molecular systems, seeking an optimal NMR calculation methodology. The library of molecular compounds include oxo- and isoelectronic imidovanadium(V) complexes with both Cl- and O-based anionic ligands: $V(=E)Cl_{3-x}(OEt)_x(bipy)$ (E = O, NR, x = 0 or 1) to explore the effect of σ-donation and to cover a broad range of chemical shifts.

The ^{51}V solution NMR spectra reveal a dramatic change in δ_{iso} spanning from 330 ppm (E = NDipp) to -6 ppm (E = N*t*Bu) within the isostructural $V(=NR)Cl_3(bipy)$ series, the oxo counterpart being at -101 ppm for (E = O), clearly illustrating the effect of stronger σ-donor ligands. Conversely, substitution of chloride for ethoxide ligands resulted in systematic shielding of isotropic chemical shift, yielding from -101 to -400 ppm for $VOCl_3(bipy)$ and $VOCl_2(OEt)(bipy)$ respectively. DFT calculations on this molecular library were next carried out using the B3LYP[38-39] density functional and the Def2TZVP[40-41] basis set accounting for relativistic effects using the zeroth order relativistic approximation (ZORA). The NMR calculations show a satisfactory correlation between calculated σ_{iso} and experimental δ_{iso} (Figure 2), illustrating that the calculated electronic structures are well-reproduced (For calculation method screening, see ESI). Note that the experimental δ_{iso} obtained by solid-state NMR are systematically shifted to lower ppm values, this is likely due to the concentration dependence of the reference. The calculated chemical shielding can therefore be related to the chemical shift through $\delta = -2128 - \sigma$ ppm and $\delta = -2091 - \sigma$ ppm in solution (C_6D_6) and solid-state, respectively (All further NMR calculations are referenced to the solution NMR data). Furthermore, comparing the calculated span and skew to the experimentally determined ones extracted from the solid-state NMR data further provides evidence for the accuracy of the calculations. For instance, the measured and calculated span (534 vs. 446 ppm) and skew (0.6 vs. 0.5) of $VOCl_2(OEt)(bipy)$ are in rather good agreement considering the large chemical shift window and the absence of intermolecular interactions in the DFT models. This further shows that the chosen NMR calculation methodology is appropriate and that the level of theory provides a reasonable description of the electronic structure of the vanadium sites.

Next, we modeled the V-surface sites in $VOCl_3@MgCl_2(thf)_{1.5}$, by adsorbing $VOCl_3$ on various undercoordinated Mg surface sites, obtained by cleaving along crystallographic planes (110) and (104) of crystalline $MgCl_2$. The unit cells were subsequently expanded orthogonally by adding a vacuum slab to the cleaved plane to avoid interactions between neighboring unit cells. The models were constructed by interacting $VOCl_3$ with the various surfaces followed by an optimization of the geometry using periodic DFT (For computational details, see ESI). Neutral clusters containing two to three coordination shells were cut from the periodic models to calculate NMR parameters using atomic orbital basis sets as for molecular analogs, reoptimizing the first coordination shell around vanadium using B3LYP/Def2TZVP (Figure 3a). The investigated surfaces were chosen to contain 5- and 4-coordinated Mg surface sites to represent different degrees of unsaturation (Figure 3b). The resulting models showed a

multitude of interactions between $VOCl_3$ and the (110) and (104) planes of $MgCl_2$ depending on the starting orientation of $VOCl_3$, reminiscent of the reported interactions with $TiCl_4$.[13, 17, 37, 42-44] No interaction to the (001) plane of $MgCl_2$ was observed, which is unsurprising as the interaction is driven by undercoordinated Mg ions that are not present on this surface. While intrinsically incomplete as restricted to a specific crystalline material, four representative models were selected, two based on the (104) plane and two based on the (110) plane (Figure 3c). Models based on the step-like defect of the (104) facet were also considered but discarded based on their calculated NMR signature (ESI). Among the various models, the vanadium center interacts with the surface in the models through either a single chlorine ligand (**1**), two chlorine ligands (**2**), four chlorine ligands (**3**), or the oxo ligand (**4**) and vanadium adopts various geometries: distorted octahedral (Figure 3c **3**), trigonal bipyramidal (Fig. 3c **2**) and tetrahedral (Figure 3c **1** and **4**).

Furthermore, considering that previous reports had shown the presence of alkoxide ligands coordinated to Ti upon the reaction of $MgCl_2(thf)_{1.5}$ and $TiCl_4$,[14] we also extended our library substituting Cl ligands by OMe, used as representative alkoxide ligands (Figure 3c). Three different levels of alkoxylation were considered for the surface species **3**, with zero (**3a**), one (**3b**), or two OMe (**3c**) ligands**,** respectively.

Finally, to extend the library of computational models towards amorphous surfaces, models based on $MgCl_2$ nanoribbons[45] were included. These models are considered amorphous based on their lack of long-range order in more than one dimension, the term amorphous will be used synonymously with diffraction amorphous thereafter. These models were constructed by only conserving the very top layer from each model and optimizing their geometry. Models based on the (110) facet of $MgCl_2$ naturally formed the previously observed nanoribbons including a vanadium moiety (Figure 3 c, **5**). The amorphization, which can be described as a displacement of the surrounding magnesium and chlorine ions, leads to a vanadium site with a distorted octahedral geometry.

Next, the NMR parameters were calculated for each model of $VOCl_3$@$MgCl_2(thf)_{1.5}$. To deconvolute the influence of the different structural and electronic parameters, the trends within each subset were explored separately. The chemical shifts were referenced to the library of molecular compounds described previously (*vide supra*, Figure 2).

NMR Signatures of V Sites: Effect of Adsorption Sites.

Starting from models that address $VOCl_3$ adsorbed on different sites (**1-4**), all chemical shift tensors show a common orientation. The most deshielded principal component δ_{11} is always oriented along V-O_{oxo}, while δ_{22} and δ_{33} are oriented orthogonal to V-O_{oxo} with their exact orientation depending on the number of terminal ligands. This allows for a direct investigation of the amount and bonding of terminal ligands through δ_{11}. The calculated chemical shift anisotropy reveals a dependence of the chemical shift on the local geometry; this is particularly evident for the most deshielded component of the chemical shift tensor, δ_{11}. For models **1**, **2,** and **4** which exhibit a tetrahedral or distorted trigonal bipyramidal geometry at the V site, a significant deshielding of the δ_{11} parameter was observed (δ_{11} = 431-433 ppm), leading to overall very large spans ($\Omega = \delta_{11} - \delta_{33}$) of around 900 ppm, which is not consistent with the experimentally observed spectrum (330 ppm). This is in sharp contrast to what was observed for the model displaying an octahedral geometry at the V-site with δ_{11} = 83 ppm and Ω = 504 ppm, a span far closer to the experimental value (vide supra). This set of data already indicates that the observed V-sites are likely to have a near octahedral geometry. Moreover, the calculated range of (^{51}V) isotropic chemical shifts (Figure 4a **2-4**) – between -155 to -200 ppm – are shifted downfield compared to the experimentally observed isotropic chemical shift of -395 ppm, clearly indicating that the vanadium oxo surface species are not likely bound to only Cl ligands, paralleling what has been described for Ti[14] and what has been observed in the molecular library discussed prior.

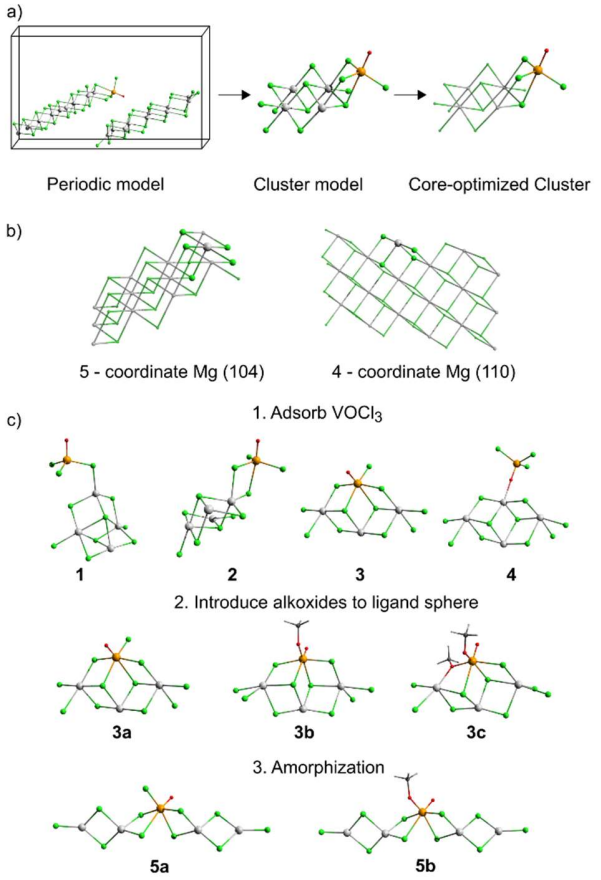

Figure 3. a) Preparation of the hybrid models from a periodic model without restrictions to a cluster with a reoptimized core around the active metal site. b) Models of surface sites of pristine $MgCl_2$ are categorized by the coordination number of the surface magnesium atoms. c) Collection of resulting cluster models used in this study. (Magnesium is shown in grey, chlorine in green, vanadium in orange, and oxygen in red)

NMR Signatures of V Sites: Effect of Ligand Substitutions.

One may note that replacing chloride for alkoxide ligands in the series of molecular complexes, used for benchmarking, results in a gradual up-field shift of δ_{iso} both in calculations and experiments. In fact, a similar trend was observed for the model surface species **3a-c**, namely a decreasing V isotropic chemical shift from –200 to –445 to –508 ppm (Figure 4b) with an increasing number of alkoxide ligands. Furthermore, the span first decreased from 504 ppm to 322 ppm for models **3a** and **3b** before rising again to 446 ppm for model **3c**. Comparing to the experimentally observed δ_{iso} of -395 ppm and span of 330 ppm,

the model with a single alkoxide ligand (**3b**) in the V-coordination environment comes closest to the experimental value with only a deviation of 49 ppm, 195 and 113 ppm for the fully chlorinated and dialkoxide environment. These results point to the presence of one alkoxide ligand in the vanadium coordination environment. Overall, these calculations already indicate that the vanadium surface sites contain one alkoxide ligand and are of near octahedral geometry. Yet even though model **3b** is in a reasonable agreement with the experiment considering the isotropic chemical shift and the span ($\Omega = \delta_{11}-\delta_{33}$), the calculated skew ($\kappa = 3(\delta_{22}-\delta_{iso})/\Omega$) of 0.44 for **3b** is significantly different from the experimentally observed value ($\kappa = 0.69$), indicating that additional local features drive the chemical shift, in particular δ_{22}.

NMR Signatures of V Sites: Effect of Surface Amorphization

Upon coordination of $VOCl_3$ or $VOCl_2(OR)$ species on $MgCl_2$ nanoribbons (Figure 3c **5a** and **5b**), which can be viewed as a amorphization of the $MgCl_2$ surface (loss of long range order beyond 2 nm), the isotropic chemical shift and span remain almost unchanged, while δ_{22} is shifted from –397 ppm to –349 ppm, leading to an increase of the skew from 0.44 in the crystalline to 0.82 in the amorphous monoalkoxide model. Both models (**3b** and **5b**) deviate only slightly in terms of isotropic chemical shift (-444 ppm and -431 ppm) from one another. The calculated chemical shifts of both the crystalline and amorphous models match the experimental shift of δ_{iso} = -395 ppm closely. Considering the experimentally observed δ_{22} of –319 ppm the amorphous model represents a significant improvement over the crystalline model. δ_{11} and δ_{33} are much more comparable between both models deviating by only 15 ppm in δ_{11} and 7 ppm in δ_{33} with the nanoribbon model matching the experimental data more closely in these parameters as well (Figure 4c).

Overall, the observed V-NMR signatures and associated NMR parameters (chemical shift principal components and related anisotropy) combined with the detailed analysis based on the computational models exploring the effect of coordination, type of anionic ligands and adsorption sites–are consistent with the formation of a hexacoordinated vanadium surface species, containing one alkoxide in its ligand coordination sphere adsorbed on a disordered (amorphous) support.

Discussion

Notably, each principal component of the chemical shift tensors provides key information regarding the structure of the vanadium sites – coordination numbers, types of ligands and detailed geometry distortion – that enables to clarify the coordination environment around the V sites.

Across the series of model systems, the calculated chemical shift tensors are essentially oriented similarly, hence the possible direct comparison of their principal tensor components (Figure 4d). As discussed above, δ_{11} is oriented along the V-O_{oxo} bond, orthogonal to the terminal anionic ligand(s). δ_{22} is oriented perpendicular to the V-O_{oxo} bond and along the bond to the terminal anionic ligand, while δ_{33} is per definition oriented orthogonal to the other two components. From the orientation of this tensor, one can already understand that changing the terminal anionic ligand (chloride vs. alkoxide) will be reflected in δ_{11}, while changes to the V-O_{oxo} bond (associated with a *trans* effect) will affect δ_{22}. This further supports the need for a more detailed analysis of the chemical shift tensor components to obtain a molecular-level understanding of the observed trends and relate local coordination environment to specific NMR signatures and electronic structure.

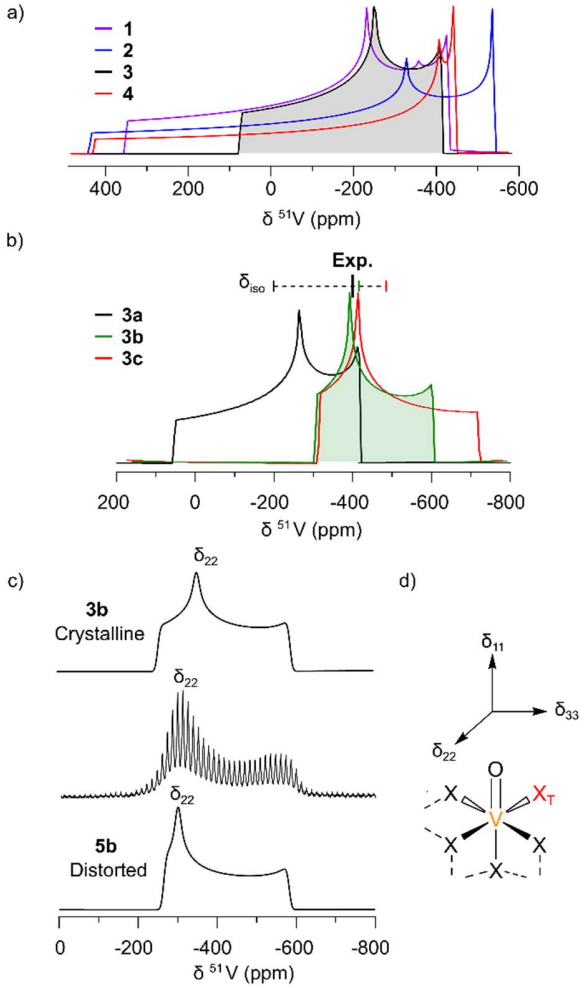

Figure 4. a) Calculated spectra of surface species with tetra-, penta- and octahedral geometry on different facets of $MgCl_2$. Only the model with octahedral geometry (3 shown in grey) has a small enough span to fit the experimental spectrum (Ω= 330 ppm). b) Calculated spectra of $VOCl_{3-x}(OR)_x$ adsorbed on the (110) surface of $MgCl_2$. Only the δ_{iso} of the monoalkoxide complex highlighted in green fits the experimental spectrum. c) Calculated spectra and models of an octahedrally coordinated monoalkoxide species before (top) and after (bottom) amorphization. The major change to the calculated NMR line is the deshielding of the δ_{22} parameter upon amorphization. d) General orientation of the ^{51}V chemical shift tensor for octahedral geometries.

The chemical shift or chemical shielding is mostly affected by changes in the paramagnetic term (σ_{para}),[46] that originates from the coupling through the angular momentum operator $\hat{L}_{k,i}$ of specific frontier molecular orbitals. According to the Ramsey equation,[47-48] these MOs need to be of adequate symmetry and close in energy (eq. 1); they can be identified via natural chemical shift (NCS) analysis. [46, 49-50]

$$\sigma_{para,ij} = -\frac{1}{2c^2}\sum_n \sum_k \frac{1}{E_n - E_0} \langle \Psi_0 | \hat{L}_{k,i} | \Psi_n \rangle \left\langle \Psi_n \left| \frac{\hat{L}_{k,j}}{r_k^3} \right| \Psi_0 \right\rangle \qquad (1)$$

The Origin of the Chemical Shift: The Effect of the Adsorption Sites

Looking first at the effect of the different adsorption sites on crystalline facets, a significant difference in isotropic chemical shift and span (δ_{11}–δ_{33}), mostly driven by changes in δ_{11}, was observed in the calculated ^{51}V-NMR signatures amongst the various models. This difference parallels the change of the vanadium site local geometry: hexacoordinated V sites have significantly smaller span than the tetra- and penta-coordinated sites.

NCS analysis of models with multiple terminal Cl ligands shows that the main contributions to the increased deshielding for δ_{11} are the V-Cl σ-bonds *cis* to the V-O_{oxo} bond that couple with low lying π*(V-Cl) antibonding orbitals by symmetry; the deshielding is significantly larger for terminal than bridging Cl-ligands and thus directly relates to the number of terminal Cl-ligands of appropriate symmetry and the geometry of the V-sites, hence the similar values of δ_{11} for models **1**, **2** and **4**. For **3** which matches the experimental spectrum best, and more general hexacoordinated V sites, the largest contribution to δ_{11} is associated with the coupling between the π(V-$Cl_{Terminal}$) and the respective σ*(V-Cl), leading to a significantly lower deshielding δ_{11} and consequently smaller span (Figure 5a). Overall, the small span observed experimentally confirms that the vanadium species generated upon adsorption of $VOCl_3$ onto $MgCl_2$ has to be hexacoordinated.

The Origin of the Chemical Shift: The Effect of the Coordination Environment

As discussed above, the substitution of anionic Cl ligands around V by alkoxide ligands in models **3a-c** has the most effect on the isotropic chemical shift and is less specific to a specific principal component (Figure 5b). The orientation of the chemical shift tensor does not significantly change upon substitution of Cl ligands, and the observed changes in the different principal components strongly depend on the position of the substituted ligand. NCS analysis shows that the main contributions to δ_{iso} in models **3a** and **3b**, are ascribed to the π (V-Cl/OR) bond of the terminal ligand, that couples to the symmetry appropriate virtual orbital of σ-antibonding character, resulting in a deshielding of δ_{11}. Deshielding is greater for models with chloride rather than methoxide ligands because of the lower electronegativity of chloride vs. oxygen-based ligands, hence the lower energy gap between the π and σ* orbitals and larger deshielding (Figure 5b). The observed more shielded isotropic chemical shift thus supports the presence of one alkoxide ligand in coordination environment of the surface species resulting from the adsorption and reaction of $VOCl_3$ on/with $MgCl_2(thf)_{1.5}$.

The Origin of the Chemical Shift: The Effect of Surface Amorphization.

The subtle changes in geometry of the V sites – associated with the structure of $MgCl_2$, i.e. adsorption of $VOCl_3$ on the (110) facet of crystalline $MgCl_2$ vs. $MgCl_2$ nanoribbon; the latter describing an amorphization of the support (Figure 5c), mostly induce changes in δ_{22}, oriented orthogonal to V-O_{oxo}. δ_{22} is more shielded in the crystalline model and is significantly different from δ_{11}, contrasting with the amorphous model. This difference results in a larger skew of 0.44 vs. 0.82 for the crystalline vs. amorphous model. Noteworthily, the observed changes in δ_{22} are due to rather subtle changes in the first coordination sphere around V. The bond angles deviate by less than 1° between the models, and the V-Ligand bond lengths are almost unaffected by the amorphization of the crystalline (V-O_{oxo} = 1.55 Å, V-OR = 1.71 Å and V-Cl = 2.37, 2.40, 2.57 and 2.88 Å) to the amorphous model (V-O_{oxo} = 1.55 Å, V-OR = 1.72 Å and V-Cl = 2.37, 2.40, 2.55 and 2.82 Å). The largest observed difference was the increase of the bond distance between V and the Cl trans to the V-O_{oxo} bond, in the case of the nanoribbon support. NCS analysis on δ_{22} revealed the π-V-O_{oxo} to σ* V-O_{oxo} transitions as the main driver of the observed changes in δ_{22} followed by σ V-O_{oxo} to π* V-O_{oxo}, albeit moving in the other direction (Figure 5c). The calculated energy difference between π-V-O_{oxo} and σ* V-O_{oxo} is smaller for the amorphous than for the crystalline model, consistent with the decreased shielding of δ_{22}. This is also reflected in the longest V-Cl bond distance, which is increased in the amorphous model, as the absence of the underlying crystal allows increased structural flexibility resulting in a decreased V-Cl interaction in favor of an increased V-O interaction. The distinct differences in the calculated NMR signature of such surface sites can only be satisfied through an amorphization of the existing models resulting in an updated geometrical model of metal surface sites in ZNCs.

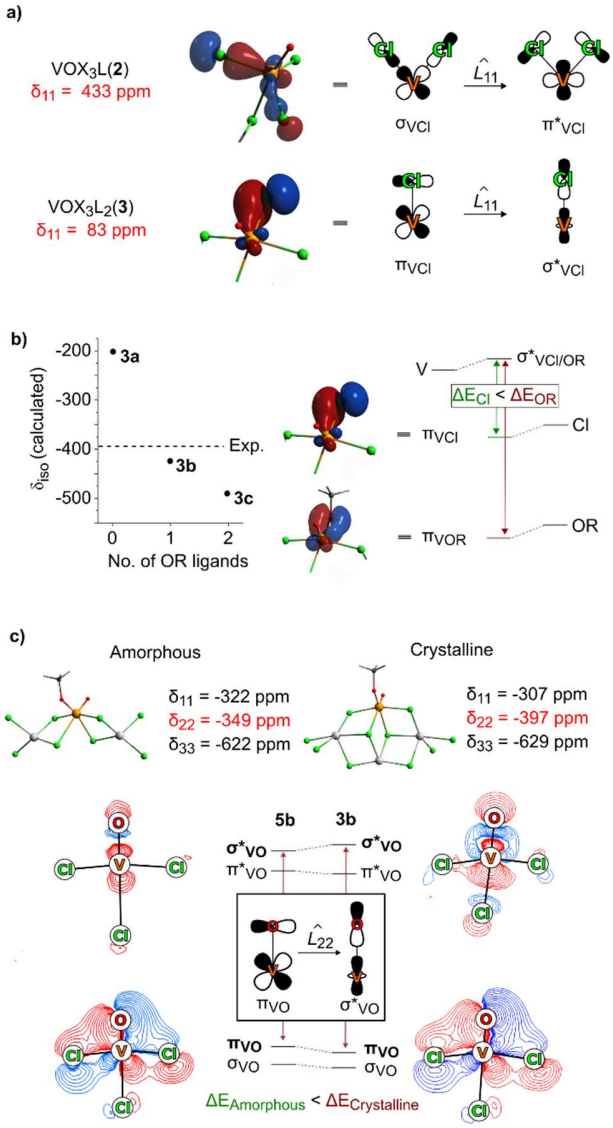

Figure 5. a) Molecular orbitals of surface species with one or several terminal ligands contributing to δ_{11} and their respective vacant orbitals of appropriate symmetry. b) Calculated isotropic chemical shifts of hexacoordinated surface species. With increasing substitution of chlorine for methoxide the shift is decreased due to the increased energy gap between the π-bonding

and σ-antibonding orbitals. c) Structural models of the crystalline and amorphous monoalkoxide surface sites and their calculated NMR parameters. Topographical representation of the molecular orbitals determined through NCS analysis to affect δ_{22} and schematic representation of the differences in the energy diagram between both models.

Conclusion

^{51}V solid-state NMR, when combined with computational models, provides a powerful tool to analyze the structure of surface sites in V-ZNC. We show that the NMR signatures of V are very sensitive to the coordination number, the presence of specific ligands and the local geometry imposed by the support. We show that, upon adsorption of $VOCl_3$, the support – $MgCl_2(thf)_{1.5}$ – is greatly modified and participates in shaping the coordination environment around V. First, as previously reported based on ^{13}C NMR on the corresponding Ti-systems, THF reacts with the metal sites to generate alkoxy species which bind to the metal center. In addition, during that step, the structure of the support is greatly modified, moving from crystalline to amorphous. While it was already known from X-Ray diffraction studies, it is clearly reflected in the ^{51}V NMR signature, which is consistent with an amorphous adsorption environment. Yet, one should point out that the V sites display a quite unique NMR signature, which demonstrates the homogeneity of surface sites consistent with the almost uniform nature of the surface sites upon activation with $AlEt_3$. This information should clearly be considered when trying to elucidate the structure of the corresponding Ti-based catalysts. Following our recent work on Ti-NMR,[28] quadrupolar NMR seems to be privileged to enable distinguishing specific surface sites even for the more challenging Ti-based ZNCs.[51]

ASSOCIATED CONTENT

The supporting information containing synthetic procedure, characterization and spectroscopic data on all the supported/molecular materials, and calculation details is available free of charge.

AUTHOR INFORMATION

Corresponding Author

Christophe Copéret - Department of Chemistry and Applied Biosciences, ETH Zürich, Vladimir-Prelog-Weg 2, CH-8093 Zürich, Switzerland, Email: ccoperet@ethz.ch

Authors

‡ S.S. and Y.K. have contributed equally.

Funding Sources

C.C., Y.K. and S.R.D. acknowledge the Swiss National Science Foundation (grants 200021_169134 and 200020B_192050). C.C. and A.Y. thank the ETH+ program (SynMatLab) for financial support.

ACKNOWLEDGMENT

All simulations were performed on the ETH-Zürich Euler cluster. C.C. is grateful to Drs. V. Monteil and J. Raynaud for fruitful discussions on the related Ti-based systems.

ABBREVIATIONS

ssNMR, solid-state NMR; CS, Chemical Shift; ZNC, Ziegler-Natta catalyst; CSA, Chemical shift anisotropy; NMR, Nuclear magnetic resonance; DFT, Density functional theory; C_Q, Quadrupolar coupling constant; η, asymmetry factor; δ, chemical shift; σ, chemical shielding; Ω, span; κ, skew; WURST, wideband uniform rate smooth truncation; QCPMG, Quadrupolar Carr Purcell Meiboom Gill; IUPAC, International union of pure and applied chemistry; XRD, X-ray diffraction; EFG, Electric field gradient; MAS, Magic angle spinning; B3LYP, Becke 3-parameter Lee-Yang-Parr; PBE, Perdew-Burke-Ernzerhof; VASP, Vienna ab initio simulation package; ADF, Amsterdam density functional; NCS, Natural chemical shift; NLMO, Natural localized molecular orbital;

REFERENCES

1. Kashiwa, N., The discovery and progress of MgCl2-supported TiCl4 catalysts. *J. Polym. Sci., Part A: Polym. Chem.* **2004,** *42* (1), 1-8.
2. Czaja, K.; Białek, M., Vanadium-based Ziegler-Natta catalyst supported on MgCl2(THF)2 for ethylene polymerization. *Macromol. Rapid Commun.* **1996,** *17* (4), 253-260.
3. Kukalyekar, N.; Balzano, L.; Peters, G. W.; Rastogi, S.; Chadwick, J. C., Characteristics of Bimodal Polyethylene Prepared via Co-Immobilization of Chromium and Iron Catalysts on an MgCl2-Based Support. *Macromol. React. Eng.* **2009,** *3* (8), 448-454.
4. Huang, R.; Liu, D.; Wang, S.; Mao, B., Spherical MgCl2 supported iron catalyst for ethylene polymerization: effect of the preparation procedure on catalyst activity and the morphology of polyethylene particles. *Macromol. Chem. Phys.* **2004,** *205* (7), 966-972.
5. Huang, R.; Duchateau, R.; Koning, C. E.; Chadwick, J. C., Zirconocene Immobilization and Activation on MgCl2-Based Supports: Factors Affecting Ethylene Polymerization Activity. *Macromolecules* **2008,** *41* (3), 579-590.
6. Vittoria, A.; Meppelder, A.; Friederichs, N.; Busico, V.; Cipullo, R., Demystifying Ziegler–Natta Catalysts: The Origin of Stereoselectivity. *ACS Catal.* **2017,** *7* (7), 4509-4518.
7. Soga, K.; Shiono, T., Ziegler-Natta catalysts for olefin polymerizations. *Prog. Polym. Sci.* **1997,** *22* (7), 1503-1546.
8. Kaminsky, W., *Polyolefins: 50 years after Ziegler and Natta I Polyethylene and Polypropylene*; Springer Berlin Heidelberg, 2013.
9. Seth, M.; Margl, P. M.; Ziegler, T., A Density Functional Embedded Cluster Study of Proposed Active Sites in Heterogeneous Ziegler−Natta Catalysts. *Macromolecules* **2002,** *35* (20), 7815-7829.
10. Bolton, P. D.; Mountford, P., Transition metal imido compounds as Ziegler–Natta olefin polymerisation catalysts. *Adv. Synth. Catal.* **2005,** *347* (2-3), 355-366.
11. Zhao, Z.; Mikenas, T.; Zakharov, V. A.; Nikolaeva, M.; Matsko, M.; Bessudnova, E.; Wu, W., Copolymerization of ethylene with α-olefins over highly active supported Ziegler-Natta catalyst with vanadium active component. *Polyolefins J.* **2019,** *6* (2), 117-126.
12. Wang, D.; Zhao, Z.; Mikenas, T.; Lang, X.; Echevskaya, L.; Zhao, C.; Matsko, M.; Wu, W., A new high-performance Ziegler–Natta catalyst with vanadium active component supported on highly-dispersed MgCl2 for producing polyethylene with broad/bimodal molecular weight distribution. *Polym. Chem.* **2012,** *3* (9), 2377-2382.
13. Credendino, R.; Busico, V.; Causà, M.; Barone, V.; Budzelaar, P. H.; Zicovich-Wilson, C., Periodic DFT modeling of bulk and surface properties of MgCl2. *Phys. Chem. Chem. Phys.* **2009,** *11* (30), 6525-6532.
14. Grau, E.; Lesage, A.; Norsic, S.; Copéret, C.; Monteil, V.; Sautet, P., Tetrahydrofuran in TiCl4/THF/MgCl2: a Non-Innocent Ligand for Supported Ziegler–Natta Polymerization Catalysts. *ACS Catal.* **2013,** *3* (1), 52-56.
15. D'Anna, V.; Norsic, S.; Gajan, D.; Sanders, K.; Pell, A. J.; Lesage, A.; Monteil, V.; Copéret, C.; Pintacuda, G.; Sautet, P., Structural Characterization of the EtOH–TiCl4–MgCl2 Ziegler–Natta Precatalyst. *J. Phys. Chem. C* **2016,** *120* (32), 18075-18087.
16. Ashuiev, A.; Humbert, M.; Norsic, S.; Blahut, J.; Gajan, D.; Searles, K.; Klose, D.; Lesage, A.; Pintacuda, G.; Raynaud, J.; Monteil, V.; Copéret, C.; Jeschke, G., Spectroscopic Signature and Structure of the Active Sites in Ziegler–Natta Polymerization Catalysts Revealed by Electron Paramagnetic Resonance. *J. Am. Chem. Soc.* **2021,** *143* (26), 9791-9797.

17. Iijima, T.; Shimizu, T.; Goto, A.; Deguchi, K.; Nakai, T.; Ohashi, R.; Saito, M., 47,49Ti solid-state NMR and DFT study of Ziegler-Natta catalyst: Adsorption of TiCl4 molecule onto the surface of MgCl2. *J. Phys. Chem. Solids* **2019,** *135*, 109088.
18. Blaakmeer, E. S.; Wensink, F. J.; van Eck, E. R. H.; de Wijs, G. A.; Kentgens, A. P. M., Preactive Site in Ziegler–Natta Catalysts. *J. Phys. Chem. C* **2019,** *123* (23), 14490-14500.
19. Piovano, A.; D'Amore, M.; Wada, T.; Cleto Bruzzese, P.; Takasao, G.; Thakur, A.; Chammingkwan, P.; Terano, M.; Civalleri, B.; Bordiga, S.; Taniike, T.; Groppo, E., Revisiting the identity of δ-MgCl2: Part II. Morphology and exposed surfaces studied by vibrational spectroscopies and DFT calculation. *J. Catal.* **2020,** *387*, 1-11.
20. Wada, T.; Takasao, G.; Piovano, A.; D'Amore, M.; Thakur, A.; Chammingkwan, P.; Bruzzese, P. C.; Terano, M.; Civalleri, B.; Bordiga, S.; Groppo, E.; Taniike, T., Revisiting the identity of δ-MgCl2: Part I. Structural disorder studied by synchrotron X-ray total scattering. *J. Catal.* **2020,** *385*, 76-86.
21. D'Amore, M.; Thushara, K. S.; Piovano, A.; Causà, M.; Bordiga, S.; Groppo, E., Surface Investigation and Morphological Analysis of Structurally Disordered MgCl2 and MgCl2/TiCl4 Ziegler–Natta Catalysts. *ACS Catal.* **2016,** *6* (9), 5786-5796.
22. Piovano, A.; Signorile, M.; Braglia, L.; Torelli, P.; Martini, A.; Wada, T.; Takasao, G.; Taniike, T.; Groppo, E., Electronic Properties of Ti Sites in Ziegler–Natta Catalysts. *ACS Catal.* **2021,** *11* (15), 9949-9961.
23. Stukalov, D. V.; Zakharov, V. A., Active Site Formation in MgCl2−Supported Ziegler−Natta Catalysts. A Density Functional Theory Study. *J. Phys. Chem. C* **2009,** *113* (51), 21376-21382.
24. Rodriguez, L. A. M.; Van Looy, H. M., Studies on Ziegler-Natta catalysts. Part V. Stereospecificity of the active center. *J. Polym. Sci., Part A: Polym. Chem.* **1966,** *4* (8), 1971-1992.
25. Potapov, A. G.; Kriventsov, V. V.; Kochubey, D. I.; Bukatov, G. D.; Zakharov, V. A., EXAFS study of supported TiCl4/MgCl2 catalyst. *Macromol. Chem. Phys.* **1997,** *198* (11), 3477-3484.
26. Lapina, O. B.; Mats'ko, M. A.; Mikenas, T. B.; Zakharov, V. A.; Paukshtis, E. A.; Khabibulin, D. F.; Sobolev, A. P., 51V NMR Study of VOCl3 Immobilized on the SiO2 and MgCl2 Surface. *Kinet. Catal.* **2001,** *42* (4), 553-560.
27. Stone, N. J., Table of nuclear electric quadrupole moments. *At. Data Nucl. Data Tables* **2016,** *111-112*, 1-28.
28. Lätsch, L. M., I. B.; Hassan, A.; Perrone, B.; Aghazada, S.; Berkson , Z. J.; Yakimov , A. V.; De Baerdemaeker, T.; Parvulescu, A.-N.; Seidel, K.; Teles , J. H.; Copéret, C. , NMR Signatures and Electronic Structures of Ti-Sites in Titanosilicalite-1 from Solid-State 47/49Ti NMR Spectroscopy. *ChemRxiv* **2022**. DOI: 10.26434/chemrxiv-2022-f71c2
29. Rehder, D., Vanadium NMR of organovanadium complexes. *Coord. Chem. Rev.* **2008,** *252* (21-22), 2209-2223.
30. Butler, A.; Eckert, H., Vanadium-51 NMR as a probe of vanadium (V) coorination to human apotransferrin. *J. Am. Chem. Soc.* **1989,** *111* (8), 2802-2809.
31. Eckert, H.; Wachs, I. E., Solid-state vanadium-51 NMR structural studies on supported vanadium (V) oxide catalysts: vanadium oxide surface layers on alumina and titania supports. *J. Phys. Chem.* **1989,** *93* (18), 6796-6805.
32. Czaja, K.; Białek, M., Effect of hydrogen on the ethylene polymerization process over Ziegler–Natta catalysts supported on MgCl2(THF)2. I. Studies of the chain-transfer reaction. *J. Appl. Polym. Sci.* **2001,** *79* (2), 356-360.
33. Niyomthai, T.; Ratchadaphet, A.; Jongsomjit, B.; Praserthdam, P., Influence of Hydrogen on Catalytic Properties of Ziegler-Natta Catalysts Prepared by Different Methods in Ethylene Polymerization. *Adv. Polym. Tech.* **2018,** *37* (4), 1035-1040.
34. Larsen, F. H.; Jakobsen, H. J.; Ellis, P. D.; Nielsen, N. C., QCPMG-MAS NMR of Half-Integer Quadrupolar Nuclei. *J. Magn. Reson.* **1998,** *131* (1), 144-147.
35. O'Dell, L. A.; Schurko, R. W., QCPMG using adiabatic pulses for faster acquisition of ultra-wideline NMR spectra. *Chem. Phys. Lett.* **2008,** *464* (1), 97-102.
36. O'Dell, L. A., The WURST kind of pulses in solid-state NMR. *Solid State Nucl. Magn. Reson.* **2013,** *55-56*, 28-41.
37. D'Amore, M.; Credendino, R.; Budzelaar, P. H. M.; Causá, M.; Busico, V., A periodic hybrid DFT approach (including dispersion) to MgCl2-supported Ziegler–Natta catalysts – 1: TiCl4 adsorption on MgCl2 crystal surfaces. *J. Catal.* **2012,** *286*, 103-110.
38. Lee, C.; Yang, W.; Parr, R. G., Development of the Colle-Salvetti correlation-energy formula into a functional of the electron density. *Phys. Rev. B: Condens. Matter* **1988,** *37* (2), 785.
39. Vosko, S. H.; Wilk, L.; Nusair, M., Accurate spin-dependent electron liquid correlation energies for local spin density calculations: a critical analysis. *Can. J. Phys.* **1980,** *58* (8), 1200-1211.
40. Weigend, F., Accurate Coulomb-fitting basis sets for H to Rn. *Phys. Chem. Chem. Phys.* **2006,** *8* (9), 1057-1065.
41. Weigend, F.; Ahlrichs, R., Balanced basis sets of split valence, triple zeta valence and quadruple zeta valence quality for H to Rn: Design and assessment of accuracy. *Phys. Chem. Chem. Phys.* **2005,** *7* (18), 3297-3305.
42. Busico, V.; Causà, M.; Cipullo, R.; Credendino, R.; Cutillo, F.; Friederichs, N.; Lamanna, R.; Segre, A.; Van Axel Castelli, V., Periodic DFT and High-Resolution Magic-Angle-Spinning (HR-MAS) 1H NMR Investigation of the Active Surfaces of MgCl2-Supported Ziegler−Natta Catalysts. The MgCl2 Matrix. *J. Phys. Chem. C* **2008,** *112* (4), 1081-1089.
43. Kresse, G.; Joubert, D., From ultrasoft pseudopotentials to the projector augmented-wave method. *Phys. Rev. B: Condens. Matter* **1999,** *59* (3), 1758.
44. Blöchl, P. E., Projector augmented-wave method. *Phys. Rev. B: Condens. Matter* **1994,** *50* (24), 17953-17979.
45. Vittadello, M.; Stallworth, P. E.; Alamgir, F. M.; Suarez, S.; Abbrent, S.; Drain, C. M.; Di Noto, V.; Greenbaum, S. G., Polymeric δ-MgCl2 nanoribbons. *Inorg. Chim. Acta* **2006,** *359* (8), 2513-2518.
46. Gordon, C. P.; Lätsch, L.; Copéret, C., Nuclear Magnetic Resonance: A Spectroscopic Probe to Understand the Electronic Structure and Reactivity of Molecules and Materials. *J. Phys. Chem. Lett.* **2021,** *12* (8), 2072-2085.
47. Pyykkö, P., Perspective on Norman Ramsey's theories of NMR chemical shifts and nuclear spin–spin coupling. *Theor. Chem. Acc.* **2000,** *103* (3), 214-216.
48. Ramsey, N. F., Magnetic Shielding of Nuclei in Molecules. *Phys. Rev.* **1950,** *78* (6), 699-703.
49. Autschbach, J., Analyzing NMR shielding tensors calculated with two-component relativistic methods using spin-free localized molecular orbitals. *J. Chem. Phys.* **2008,** *128* (16), 164112.
50. Bohmann, J. A.; Weinhold, F.; Farrar, T. C., Natural chemical shielding analysis of nuclear magnetic resonance shielding tensors from gauge-including atomic orbital calculations. *J. Chem. Phys.* **1997,** *107* (4), 1173-1184.
51. Yakimov, A. V.; Kaul, C. J.; Kakiuchi, Y.; Sabisch, S.; Bolner, F. M.; Raynaud, J.; Monteil, V.; Berruyer, P.; Copéret, C., A Well-Defined Ti Surface Site in Ziegler-Natta Pre-Catalysts from High-field Low Temperature 47/49Ti solid-state NMR Spectroscopy. **2023**, *submitted for publication*.

TOC: